China Geology 7 (2024) 517−532

China Geology

Journal homepage: http://chinageology.cgs.cn
https://www.sciencedirect.com/journal/china-geology

Application of geophysical methods in fine detection of urban concealed karst: A case study of Wuhan City, China

Dao-han Liu[a, b], Lei Wang[a, b], Lei Liu[c], Jun-jie Xu[a, b,*], Jian-qiang Wu[a, b], Pan Liu[a, b]

[a] *Wuhan Center, China Geological Survey, Wuhan*, 430205, *China*
[b] *Central South China Center for Geoscience Innovation, Wuhan*, 430205, *China*
[c] *Geophysical Exploration Brigade of Hubei Geological Bureau, Wuhan* 430056, *China*

ARTICLE INFO

Article history:
Received 14 March 2023
Received in revised form 12 July 2023
Accepted 24 August 2023
Available online 16 November 2023

Keywords:
Ground Penetrating Radar (GPR)
Electric Resistivity Tomography (ERT)
Opposing-coils Transient Electromagnetic Method (OCTEM)
Microtremor Array Measurements (MAM)
Multi-channel Analysis of surface wave (MASW)
Multi-source surface wave exploration (MSSW)
Electromagnetic wave CT (EM CT)
Surface Nuclear Magnetic Resonance (SNMR)
Concealed karst
Urban geological survey engineering

ABSTRACT

The construction of modern livable cities faces challenges in karst areas, including ground collapse and engineering problems. Wuhan, with a population of 13.74×10^6 and approximately 1161 km^2 of soluble rocks in the urban area of 8569.15 km^2, predominantly consists of concealed karst areas where occasional ground collapse events occur, posing significant threats to underground engineering projects. To address these challenges, a comprehensive geological survey was conducted in Wuhan, focusing on major karst-related issues. Geophysical methods offer advantages over drilling in detecting concealed karst areas due to their efficiency, non-destructiveness, and flexibility. This paper reviewed the karst geological characteristics in Wuhan and the geophysical exploration methods for karst, selected eight effective geophysical methods for field experimentation, evaluated their suitability, and proposed method combinations for different karst scenarios. The results show that different geophysical methods have varying applicability for karst detection in Wuhan, and combining multiple methods enhances detection effectiveness. The specific recommendations for method combinations provided in this study serve as a valuable reference for karst detection in Wuhan.

1. Introduction

The construction of modern livable cities is often hindered by ground collapse and engineering problems in karst areas (Wang CS et al., 2019). Wuhan City, located in the central region of China, is a central city and a super-large city with an exceptionally advantageous transportation location. It has established 460 km of subway lines and 2783.8 km of operational bus lines. The rapid urban development has created a substantial demand for the utilization and development of underground space. However, karst collapse poses a direct threat to urban safety and has become the primary form of geological disaster in urban areas (Fig. 1). In Wuhan, there is a total area of approximately 1161 km^2 of soluble rocks, with 96% being concealed karst areas where occasional ground collapse events occurred (Fan SK, 2006; Zheng XM et al., 2019). These special karst geological problems in karst area have posed significant threats to underground engineering projects, including the construction of subway and underwater tunnels (Li SC et al., 2017; Peng JB et al., 2019). To address these issues, the China Geological Survey and Wuhan Municipal Government conducted the Wuhan Multi-factor Urban Geological Survey in 2019, with a specific focus on investigating major geological and environmental issues related to karst.

Compared to drilling, geophysical methods offer advantages in detecting concealed karst areas because of their high efficiency, non-destructiveness, and flexibility (Meng YH and Lei MT, 2019). Among these methods, the most commonly used ones are Ground Penetrating Radar (GPR), Electric Resistivity Tomography (ERT), Audio-frequency Magnetotelluric (AMT), Electromagnetic wave CT (EM CT), and microgravity methods (Chalikakis K et al., 2011; Zhang W et al., 2019). GPR accurately locates karst fissures and cavities in exposed and shallow covered karst areas (Kaufmann O and Deceuster J, 2014; Liu LB and Qian RY, 2015). ERT is the most widely used method in karst surveys (Ungureanu C et al., 2017; Zheng ZJ et al., 2019), limestone-

First author: *E-mail address*: ldhwcgs@163.com (Dao-han Liu).
* Corresponding author: *E-mail address*: 1010411757@qq.com (Jun-jie Xu).

Literary editor: Li-qiong Jia
doi:10.31035/cg2023046
2096-5192/© 2024 China Geology Editorial Office.

Fig. 1. Some photos of karst collapse in Wuhan City.

soil interface recognition (Ismail A and Anderson N, 2012), and underground river detection (Zhu et al., 2011; Gan FP et al., 2017). AMT and seismic exploration methods are better for detecting buried karst areas (Valois R et al., 2011; Wu AM et al., 2018). EM CT is frequently used for engineering karst surveys, but it requires more stringent borehole spacing, well-washing process, and wellbore materials (Li SC et al., 2015; Peng Y et al., 2016). Additionally, microgravity methods can detect shallow unfilled caves (Gambetta M et al., 2011; Solbakk T et al., 2018). Multiple geophysical methods together can improve the reliability of karst detection by obtaining multiple physical properties of karst (Chen YL et al., 2013; Eftychia A et al., 2022).

Karst exploration in Wuhan has a long history, with previous research primarily focusing on cave detection and the distribution of karst area. However, limited attention has been given to the detection of soil structure, underground karst water, and the systematic integration of rock detection methods (Fu ZY et al., 2020; Li CX et al., 2021). Consequently, there exists a deficiency in the comprehension of appropriate geophysical methods and effective exploration solutions. To bridge this gap, this paper undertook a comprehensive review of prior geological surveys and studies, thereby selecting eight geophysical methods deemed effective for field experimentation. These selected methods were subsequently evaluated for their suitability in addressing specific targets of karst exploration. Furthermore, the combinations of suitable methods were proposed to accommodate diverse stages of karst collapse development and geological scenarios.

2. Geological and geophysical characteristics of karst in Wuhan

2.1. Geological characteristics of karst in Wuhan

Wuhan City is located in the eastern part of Hubei Province, encompassing two secondary tectonic units: the Yangtze landmass region and the Qinling-Dabie orogenic belt (Fig. 2b). These two regions are separated by the Xiangfan-Guangji major fault, with the southern side constituting the fold-thrust belt of the Lower Yangtze landmass in the Yangtze landmass region. The northern side, on the other hand, comprises the Qinling arc basin system of the Qinling-Dabie orogenic belt, which includes the rift valleys of the southern margin and the Macheng-Xinzhou depression (He J et al., 2020). The karst landscape mainly occurs in the southern Platform fold-thrust belt, with a total area of about 1161 km^2, where eight east-west karst belts are developed with a width generally ranging from 0.8 km to 6.8 km and a maximum of 12 km (Fig. 2a and Fig. 2c). These karst features are predominantly located in the core of the anticline, with a smaller number present in the limb of the anticline. The karst strata primarily consist of the Triassic Jialingjiang Formation ($T_{1\text{-}2}j$)and Daye Formation (T_1d), the Middle Permian Qixia and Gufeng Formation (P_2q+g), the Carboniferous Huanglong and Dapu Formation (C_2d+h) (Fig. 2d). Table 1 provides an overview of the main karst strata and their characteristics in Wuhan.

Many scholars have analyzed the mechanisms of karst collapses in Wuhan, examining various aspects such as triggering factors, collapse modes, and evolution mechanisms (Wang F et al., 2017; Zheng XM et al., 2019). By considering the composition and transportation of the overlying soil, the karst collapses mechanisms in Wuhan have been classified into several types, including soil-cavity type, hourglass type, mudflow type, and composite karst subsidence (Luo XJ et al., 2021; Chen BD et al., 2021). It is evident that the “rock-soil-water” system plays a pivotal role in the process of karst geological activity (Wang JX et al., 2001; Liu DH et al., 2022a), directly influencing the formation and evolution of karst collapses and serving as a crucial aspect of urban

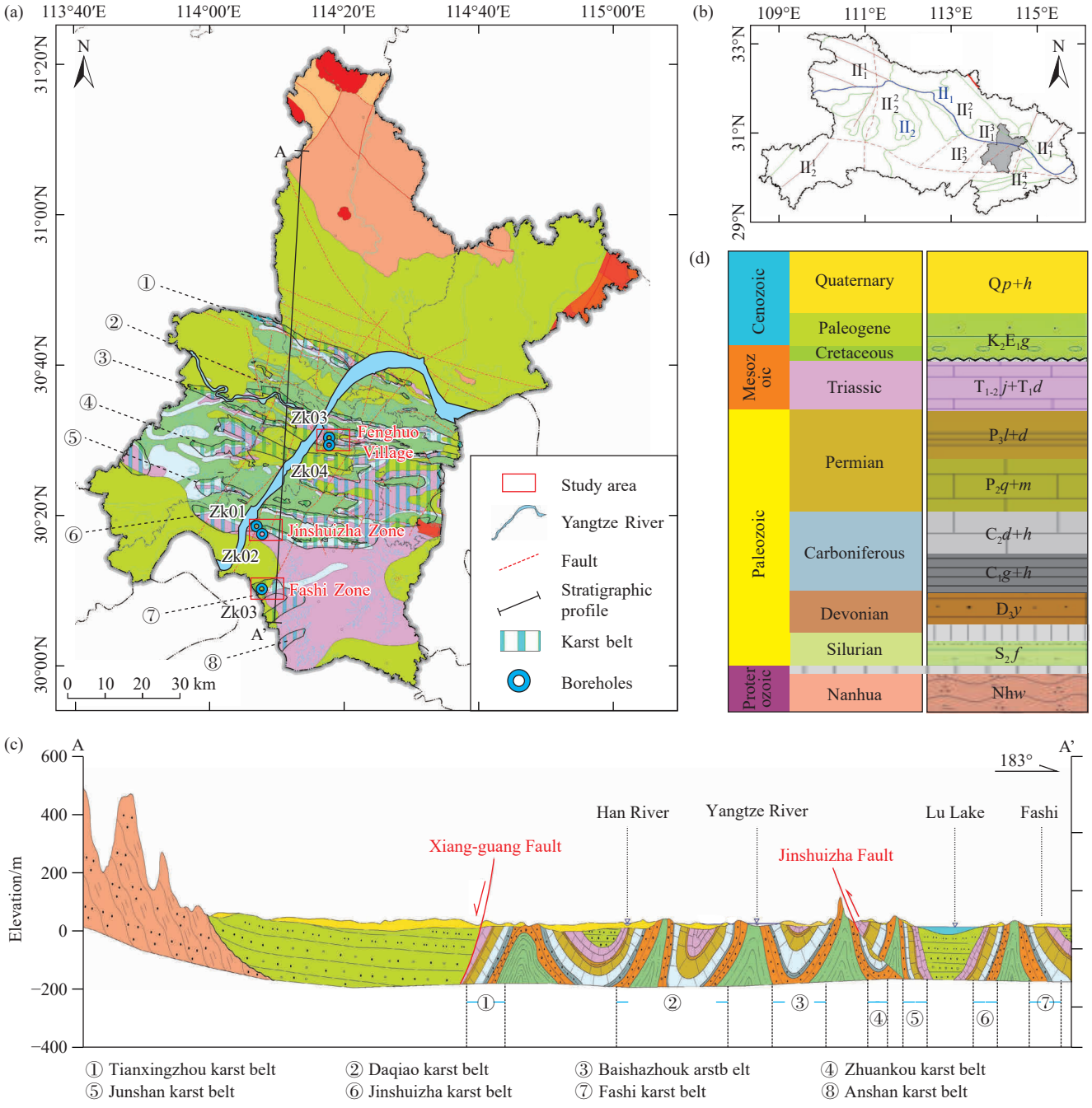

Fig. 2. Karst geological map of Wuhan City. a–bedrock geological map; b–outline map of geological structure; c–karst geological stratigraphic profile; d–geological strata map.

underground space detection. Therefore, in this paper, the characteristics of karst system have been synthesized and organized, and the specific targets for karst exploration in Wuhan have been established based on these findings (Table 2).

2.2. Geophysical characteristics of karst in Wuhan

Controlled by the first-level tectonic units on both sides of the Xiang-Guang Fault, the geophysical field in Wuhan demonstrates characteristic patterns of low gravity, strong magnetism, and low resistance in the north region, while the central and southern parts exhibit relatively higher gravity, weak magnetism, and medium to high resistance (Yan DP et al., 2015). The regional gravity field shows an overall negative anomaly in the north, primarily influenced by the Mesozoic and Cenozoic fault basins, whereas the central and southern parts exhibit a positive anomaly associated with the Mesozoic and Paleozoic strata within the region. The overall distribution aligns in an east-west direction, connected by a gradient band that follows the tectonic distribution, with the karst area arranged in a strip-like manner. The regional magnetic anomaly is predominantly influenced by sedimentary cover layers and magnetic metamorphic rocks characterized by low or weak magnetism. In the karst area, a smooth magnetic anomaly is observed, with the magnetic field displaying overall positive-negative fluctuations.

The electrical parameters for formations in Wuhan are

mainly obtained through collection and physical property samples testing. The SCIP sample rock core IP tester, produced in Canada, is used as the testing instrument. Seismic wave velocities are primarily obtained through the collection and organization of historical elastic wave logging data. Table 3 presents variations in resistivity and seismic velocity among different lithologies. Soluble rocks, clastic rocks, and soil layers exhibit distinct electrical properties, with soluble rocks having high resistivity and high velocity, and a broad range of resistivity changes that are influenced by factors like lithology, karst development, and groundwater. The loose cover layer overlying the karst area has low resistivity and low velocity. Due to the shallow groundwater burial depth in Wuhan, high-frequency electromagnetic and elastic wave energies decay rapidly, resulting in "low-resistivity shielding" and "low-velocity zone" effects, which affect the depth and resolution of geophysical exploration. Moreover, the groundwater level is impacted by the long-term fluctuations of the Yangtze River water level. The loose soil directly covering the karst top interface provides good connectivity between karst water and pore water, promoting the formation and development of karst. Most karst areas in Wuhan are filled with mud and sand, leading to the anomalous properties characterized by low resistivity and velocity, which provide a physical basis for geophysical exploration.

3. Case analysis of geophysical methods

3.1. Electric Resistivity Tomography (ERT)

ERT involves supplying a stable electric current or a very low-frequency alternating current with negligible electromagnetic effects to the subsurface. The potential difference at different electrode positions is then measured to calculate the apparent resistivity, which is further used in the inversion process to calculate the underground resistivity at different locations, allowing for the modeling of underground electrical parameters. This method combines the benefits of electrical sounding and profiling, with large data collection and high work efficiency, providing direct and accurate insights into subsurface electrical abnormal characteristics. ERT finds widespread usage in the exploration of geological structures, groundwater, karst formations, and cover layers (Yan JY et al., 2012; Verdet C et al., 2020).

3.1.1. 2D ERT

In the 2D ERT study, a comparative test of various

Table 1. Main karst strata and characteristics in Wuhan City.

System	Strata	Lithologic characteristics				Karst characteristics	
		Lithology	Structure characteristics	Calcite content	Particle size/mm	Karst phenomenon	Karst rate
Triassic	$T_{1-2}j$	Dolomite, dolomitic limestone	Developed square stone veins	-	-	Development, imbalance	1.65%–10%
	T_1d	Limestone and mudstone	Cryptocrystalline, argillaceous, granular structure	70%–95%	0.005–0.03	Relative development, dissolved gap, small caves	1.65%–10%
Permian	P_2q+m	Siliceous rock, limestone	Granular mosaic	94%–100%	0.2–2.5	Strong development, large caves	10%–30%
Carboniferous	C_2d+h	Dolomite, limestone and limestone	Hemideomorphic mosaic structure	4%–5%	0.002–0.032	Less development, cracks	1%–17%

Table 2. Characteristics of geological elements and exploration targets in Wuhan City.

Geological elements	Typical features	The main detection target
Soluble rock	1. Concealed karst predominates	1. Karst band boundaries
	2. Near east-west karst bands	2. Degree and distribution of karst
	3. Karst development at the top	3. Bedrock top interface
	4. Small caves, pores, dissolution, and sediment filling	4. Fracture and tectonic distribution
Soil	1. Multiple combination structures	1. Soil thickness
	2. Soil collapses	2. Soil structure
	3. Thickness between 30-50m	3. Soil disturbances
Groundwater	1. Shallow water level	1. Type of groundwater
	2. Strong hydraulic connection	2. Aquifer structure
	3. Mainly pressurized water	3. Aquifer water inflow

Table 3. Statistics of geophysical parameters in Wuhan city.

System	Lithology	Resistivity/Ω·m		P-wave velocity (m/s)	
		Mean	Range	Mean	Range
Quaternary	Clay, silty clay	33	21–69	371	385–698
Cretaceous	Argillaceous sandstone	94	58–232	1256	1181–1754
Triassic	Limestone and mudstone	2064	503–3750	4132	4082-4968
Permian	Limestone	907	401–1987	–	–
Carboniferous	Dolomite, limestone	1435	390–5740	3768	3185–4342
Devonian	Sandstone	286	203–437	2356	2125–3098
Silurian	Sand shale	134	72–245	1231	1300–1730

electrode space (ES) and a joint inversion of multi-array resistivity have been conducted to investigate the influence of (ES) and array configuration on karst detection in Wuhan, respectively. Geophysical profiles perpendicular to the geological structure were laid out in the Fasi-Street karst belt area, with ES values of 2 m, 5 m, and 10 m, respectively. These three ES configurations were implemented along the same profile but with varying lengths, and the overlapping positions were highlighted in red in Fig. 2. The measurement instrument used was the SuperSting R8, produced by AGI in the USA, and the data processing was performed using EarthImager2D software. The resistivity inversion results were obtained through a joint inversion of the multi-array Dipole-dipole and Schlumberger configuration.

Fig. 3 illustrates the inversion results obtained from the three ERT profiles with different ES. In all ERT profiles, the range of resistivity values is limited, ranging from 3 Ω·m to 1000 Ω·m. In principle, decreasing the ES and increasing the electrode density should enhance the lateral resolution and data quantity, thereby improving the quality of ERT imaging. For instance, the high-resistance anomalies within the red box in Fig. 3b and Fig. 3c become more distinct as the ES decreases. However, the results depicted in Fig. 3 also reveal certain distinct phenomena. For instance, the 2 m ES ERT in Fig. 3c fails to identify karst due to a flat bedrock top interface. This suggests a significant "window" effect in the imaging outcome, with the depth of resistivity inversion positively correlated with ES. Consequently, it can be inferred that a larger ES of 10 m enables rapid detection of karst belts but with lower resolution, while a smaller ES, such as 2 m, yields more focused electrical imaging, particularly for detecting internal structures of the cover layer, clay bodies, and collapse fillings in the sand layer. The 5 m ES ERT provides a good balance between the detection soil layer structures and the top bedrock's top interface in Wuhan.

To improve the conventional electrical surveying effect, the type of array used is an important parameter. Recent studies have shown that multi-array joint inversion can enhance resistivity imaging by constraining the inversion using resistivity data obtained from multi-arrays (Constantin P et al., 2019). To identify the optimal array combination for karst detection in Wuhan, this study conducted both numerical simulations and actual field measurements. In the numerical simulation, the representative karst geological structure in Wuhan was modeled, and resistivity data were generated through forward calculations, followed by the addition of 5% Gaussian noise. Subsequently, different array configurations were employed for joint inversions to evaluate the ability of the inversion results to reconstruct the initial model (Fig. 4).

The reconstruction of the electrical structure varies depending on the type of arrays employed. Among the single array types, all three are capable of delineating the electrical structure to some extent. The dipole-dipole array exhibits better performance in imaging the low-resistance "karst zone" in the central region, but the resulting resistivity values are significantly underestimated, and the high-resistance layers on both sides exhibit "blocky-like" anomalous features. In the cases of multi-arrays joint inversion, the dipole-dipole array yields a more accurate representation of the low-resistance "karst zone", and the inversion results exhibit higher

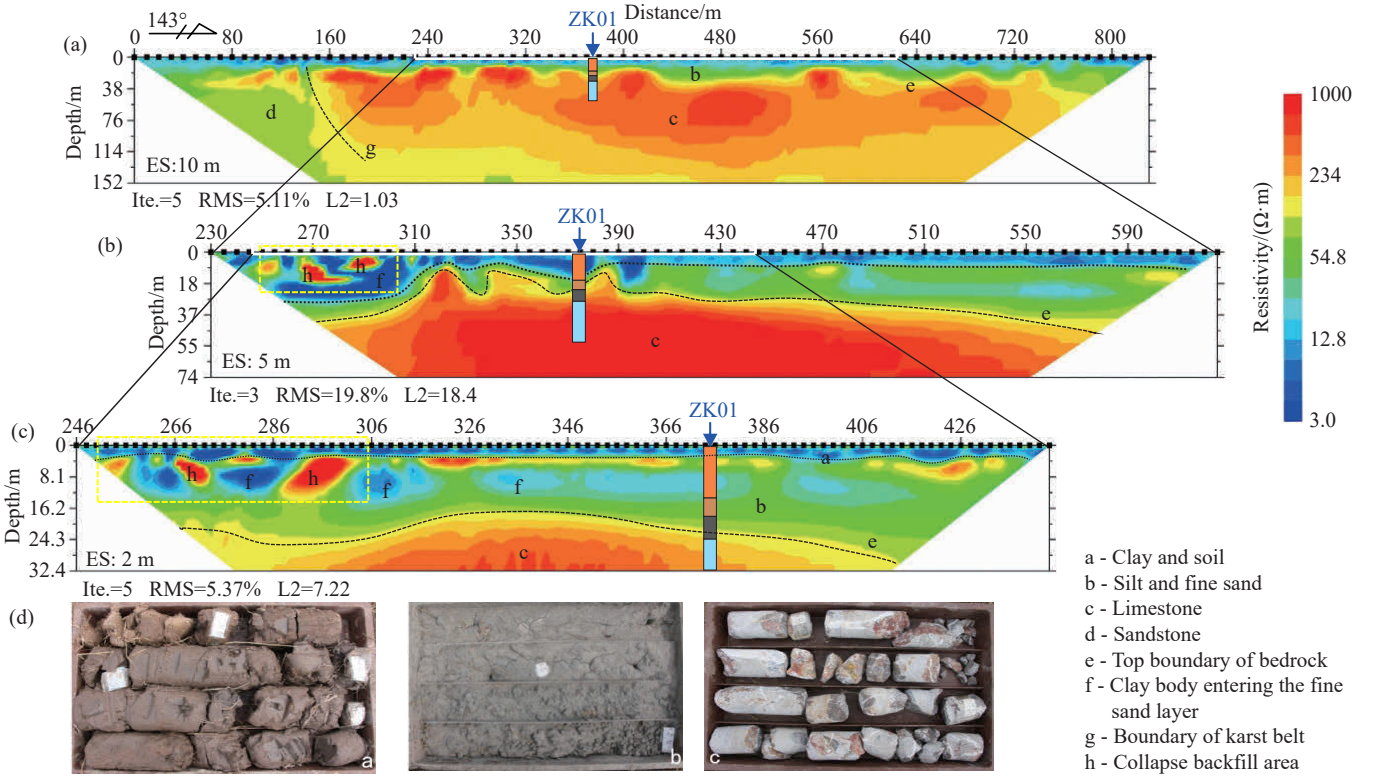

Fig. 3. Results of 2D ERT with multi-ES. a–2D ERT with 10 m ES; b–2D ERT with 5 m ES; c–2D ERT with 2 m ES; d–photographs of lithology.

similarity. However, when the schlumberger array is jointly inverted with the dipole-dipole array, it enables a more precise delineation of the top boundary of the "karst zone". Conversely, the joint inversion of the dipole-dipole and wenner arrays may result in misinterpretation due to local low-resistance anomalies during the inversion of the high-resistance surrounding rock.

This profile presents a case study of karst detection in Jinshuizha using wenner, dipole-dipole, and schlumberger arrays with a 10 m ES and 68 electrodes. The SuperSting R8 and the EarthImager2D software were utilized for data acquisition and processing. The obtained results (Fig. 5) exhibit similarities with the aforementioned numerical simulations depicted in Fig. 4. Incorporating dipole-dipole array data has significantly improved the lateral resolution and expanded the range of detectable resistivity values. This

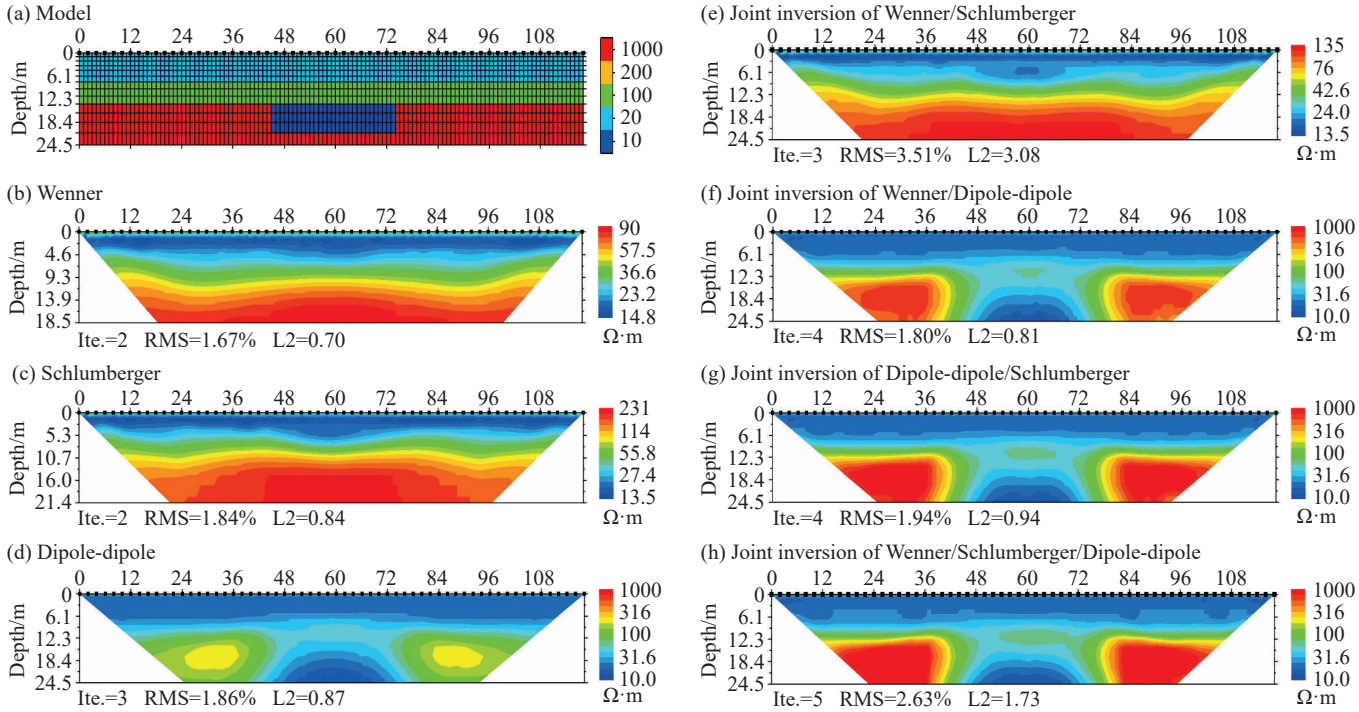

Fig. 4. Results of 2D ERT with multi-arrays joint inversion.

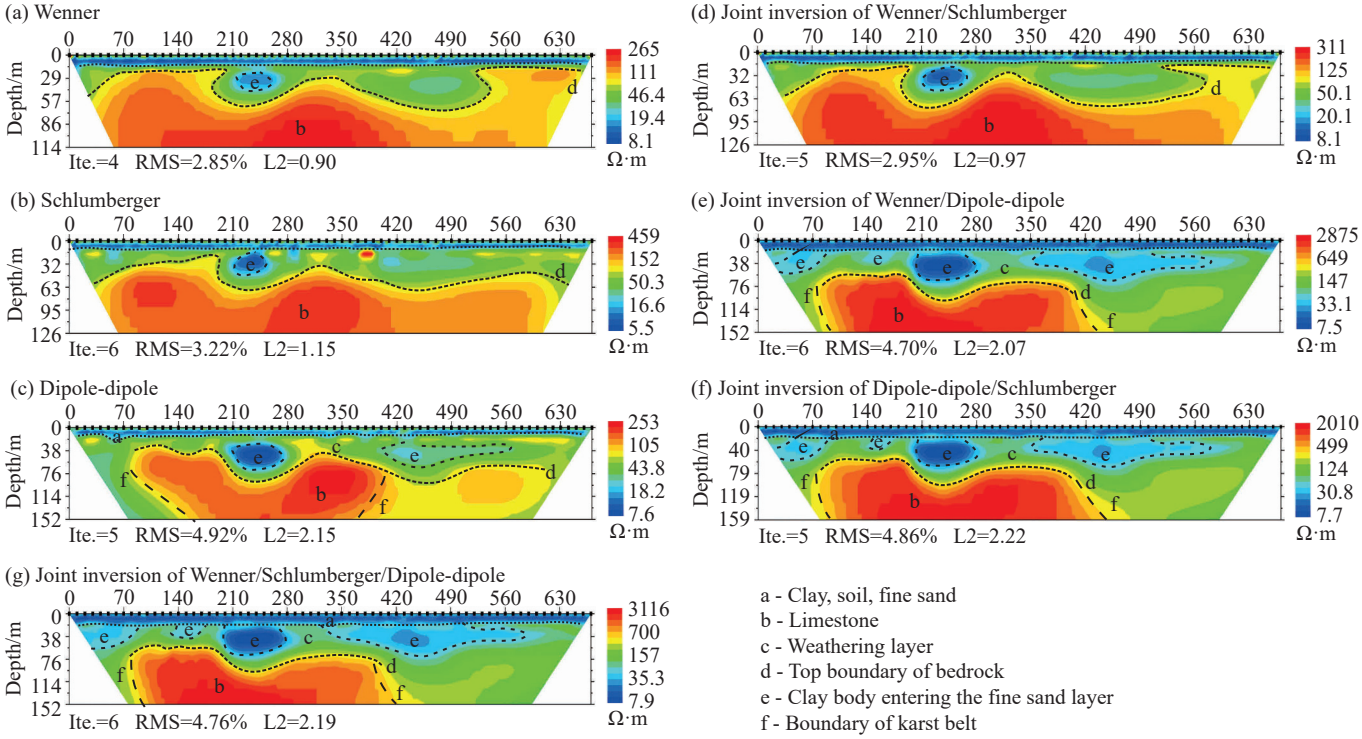

Fig. 5. Results of ERT with multi-array joint inversion in Jinshuizha karst zone.

enhancement proves valuable in distinguishing between soluble and non-soluble rocks and detecting the boundaries of karst belts. Furthermore, upon comparing the results of all types of multi-array joint inversions, it becomes evident that the joint inversion of the dipole-dipole and schlumberger arrays yields nearly identical resistivity images compared to the joint inversion involving all three arrays. Considering the time-consuming nature of wenner array measurements, which employ only one channel, and taking into account factors such as cost-effectiveness and computational efficiency, the optimized array configuration for karst detection in Wuhan is the joint utilization of the dipole-dipole and schlumberger arrays.

3.1.2. 3D ERT

This paragraph discusses the limitations of 2D ERT in detecting underground karst features and the advantages of 3D ERT. 2D ERT is limited in detecting the 3D characteristics of karst and is susceptible to false anomalies. On the other hand, 3D ERT accurately depicts the spatial 3D variation of electrical resistivity and allows for different directions of electric field excitation-reception combinations, making it advantageous in detecting 3D geological bodies especially for karst (Ismail A and Anderson N, 2012; Fu ZY et al., 2020).

The detection of underground karst channels is located on the northeast side of Shuangfeng Mountain in Huangpi District, and is a surface low-temperature hot spring group. The main spring area is located on the west side, where a large number of water ponds are formed on the surface for tropical fish farming. The three-dimensional measurement area is located on the east side near the spring outcrop, used to reveal the direction and burial depth of the underground pipelines. Data collection was carried out using 100 electrodes with a point-line spacing of 5 m × 10 m, and the collection array used was a radial dipole-gradient array. Error analysis, data elimination and three-dimensional smooth inversion were carried out on the collected apparent resistivity data, and the three-dimensional resistivity inversion results were obtained (Fig. 6).

The 3D resistivity inversion reveals that the resistivity of the surrounding rock can reach 2000 Ω·m, Furthermore, a low-resistance anomaly of approximately 50 Ω·m is observed at the central spring outcrop point. This anomaly extends as a continuous columnar body underground at a shallow depth of about 12 m. The resistivity characteristics on the plane and at different depths are illustrated in X and Z direction 2D slices, as shown in Fig. 6c–d. Fig. 6b presents the separation display of the resistivity parameter at 50 Ω·m. It can be seen that the low-resistance body extends along the SEE-NWW direction, with a trend of increasing low resistance at the lower part of the spring point and partial exposure at the surface. The main body of the low-resistance structure can still be observed extending deeper towards the NWW direction, which corresponds to the location of a larger spring group approximately 200 m away. Additionally, the resistivity detection results indicate that the underground pipeline is relatively flat and shallow. The long and shallow migration of

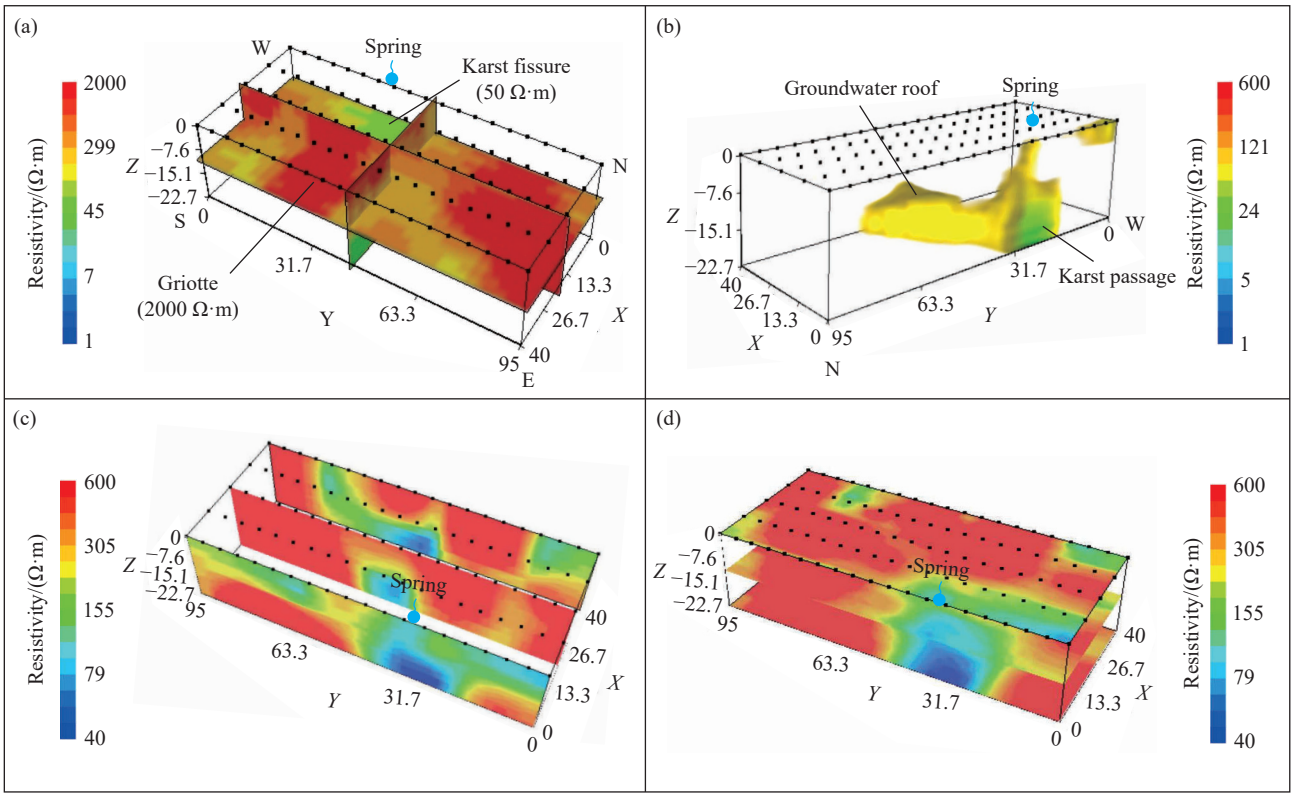

Fig. 6. Results of the spring from 3D ERT (modified from Liu et al., 2022a). a–slices inversed by 3D ERT; b–boundary of collapse body from 3D ERT; c–X direction 2D slices inversed by 3D ERT; d–Z direction 2D Slices inversed by 3D ERT.

the pipeline may be one of the contributing factors to its heat loss. In contrast to the single profile of 2D Electrical Resistivity Tomography (ERT), 3D ERT provides a comprehensive depiction of the resistivity structure across the entire detection area, facilitating the identification of spatial distribution of karst passages. Moreover, 3D ERT calculates the apparent resistivity along and perpendicular to the 2D profile direction, effectively constraining the influence of "side effects". This demonstrates the feasibility and advantages of employing 3D ERT in detecting actual karst passages. However, it is important to recognize the limitations in terms of detection scales and depths, as well as the time-consuming detection process and potential for larger fitting errors.

3.2. Surface Wave Exploration (SW)

Surface wave exploration employs multiple detectors to extract dispersion curves and investigate underground shear wave velocity structure (Wang LM et al., 2022). Currently, the passive surface wave method, particularly Microtremor Array Measurements (MAM), is widely employed to overcome the source limitations and directly extracts dispersion curves in noisy environments (Xu PF et al., 2020). Multi-source surface wave exploration (MSSW) represents an improvement over MAM, as it compensates for the high-frequency band of the dispersion image using artificial sources, thereby enhancing resolution and accuracy. MSSW has proven effective in identifying low-velocity zones and bedrock interfaces, estimating soil and rock stiffness parameters, and detecting gravel layers and bedrock covered by Quaternary soft soil (Yang WC et al., 2021).

Surface wave exploration in this study used three methods: Passive (MAM), active (MASW), and multi-sources (MSSW). As shown in Fig. 7, the schematic diagram shows the three different surface wave acquisition methods, respectively. 20 Atom seismic recorders produced by Geometrics in USA, and geophones with main frequency of 2 Hz, were used. For MAM, data were extracted from 9 linear arrays with an array spacing of 10 m and a maximum radius of 40 m, with a duration of more than 30 minutes. For MASW, the transient source from a hammer, with a minimum offset of 5 m, a trace spacing of 10 m, and a single-shot arrangement length of 80 m, a shot spacing of 10 m, a sampling rate of 4 ms, and a single-shot acquisition duration of 1s with at least 3 overlapping shots. MSSW was based on the joint re-calculation of the frequency spectra from MAM and MASW. SeisImager and Geogiga softwares were used for data pre-processing, SPAC frequency spectrum calculation, curve extraction and inversion.

Fig. 8 illustrates the comparison of dispersion spectra obtained using three different methods. The MAM dispersion spectrum primarily exhibits energy concentration between 2–7 Hz, accompanied by significant spatial aliasing. While MASW dispersion spectrum demonstrates a concentration of energy between 3–12 Hz, with relatively convergent and continuous energy clusters. Following the processing by MSSW, the frequency band capable of extracting dispersion curves extends to 2–12 Hz. Additionally, the spatial aliasing signal is effectively suppressed, thereby facilitating accurate extraction of the dispersion curves. However, it is worth noting that the high-order surface wave signals still exhibit considerable strength.

To minimize artificial factors in the inversion, the default initial models were utilized. Fig. 9 presents 2D profile results obtained by the three methods. The detection depth can reach over 90 m for MAM and MSSW， but for MASW, which was between 3–30 m, with some points less than 20 m, that was difficult to detect the bedrock depth (20–50 m) in Wuhan. In terms of vertical stratification, MASW can achieve internal stratification of the soil layer, especially in the case of large differences in velocity between the silty clay, silt and limestone, by referring to drilling data. MAM lacked high-frequency signals for shallow subsurface structures and responds poorly to changes in internal structures. While for MSSW, high-frequency enhancement was achieved, and the "blind zone" in the shallow subsurface was reduced to about 3 m, which were useful to find S wave velocity anomalies in the shallow clay. As shown in Fig. 8c, there was a distinct velocity change at 5 m depth, which indicated the interface from artificial fill to the silty clay in the borehole. MASW identified a "U"-shaped shear wave velocity anomaly band in the 380–420 m segment, which was caused by subsidence of the surface clay. MAM and MSSW showed multiple low-speed anomalies near the top interface of the limestone layer, indicating a karst development area. At 270 m, a banded low-

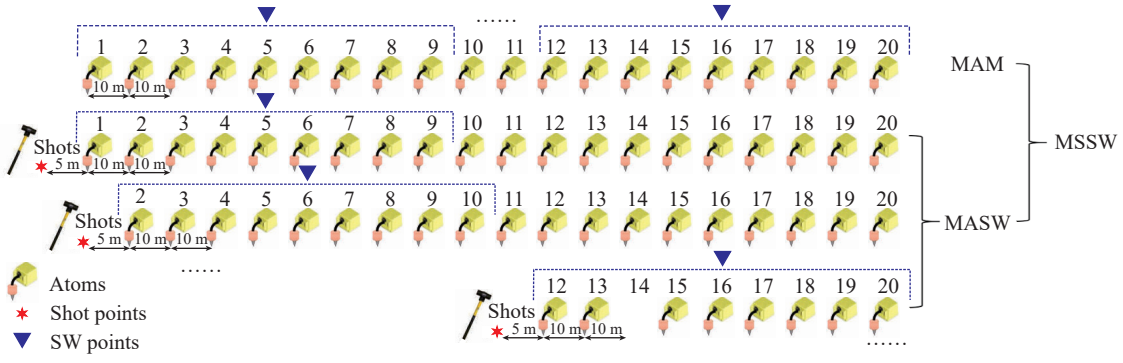

Fig. 7. Schematic diagram of three surface wave methods.

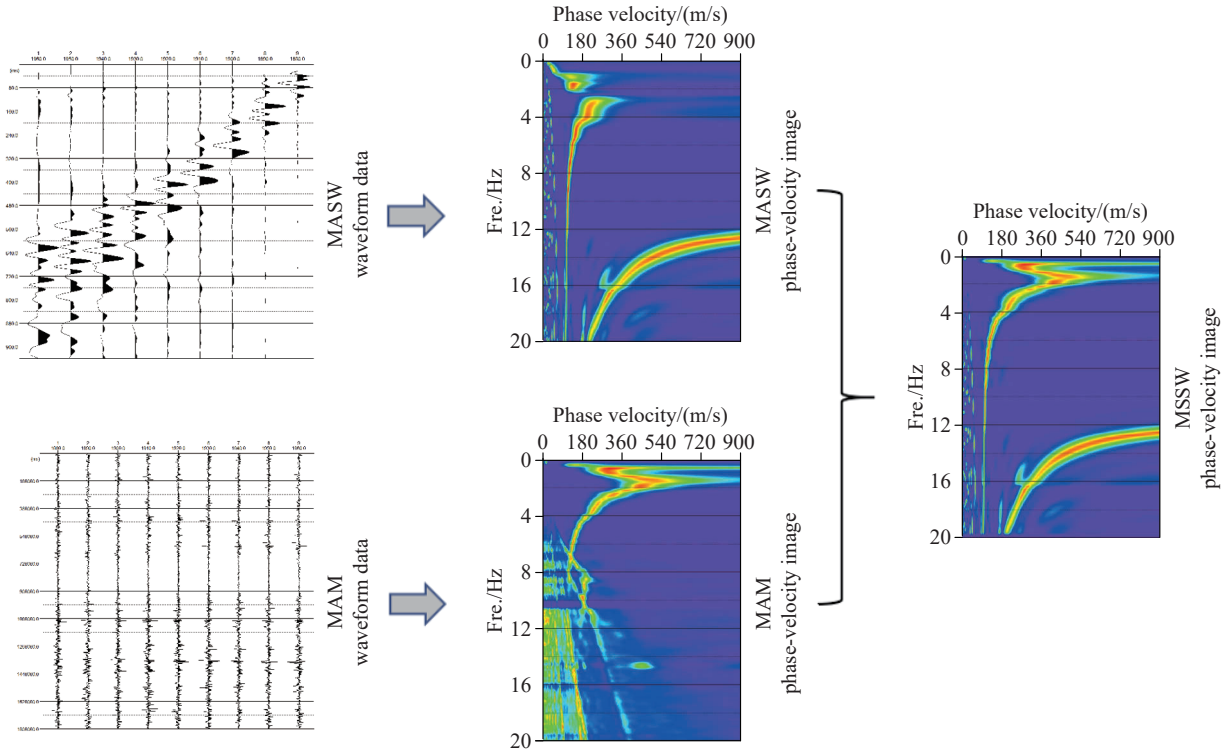

Fig. 8. Single-point spectrogram of three surface wave methods.

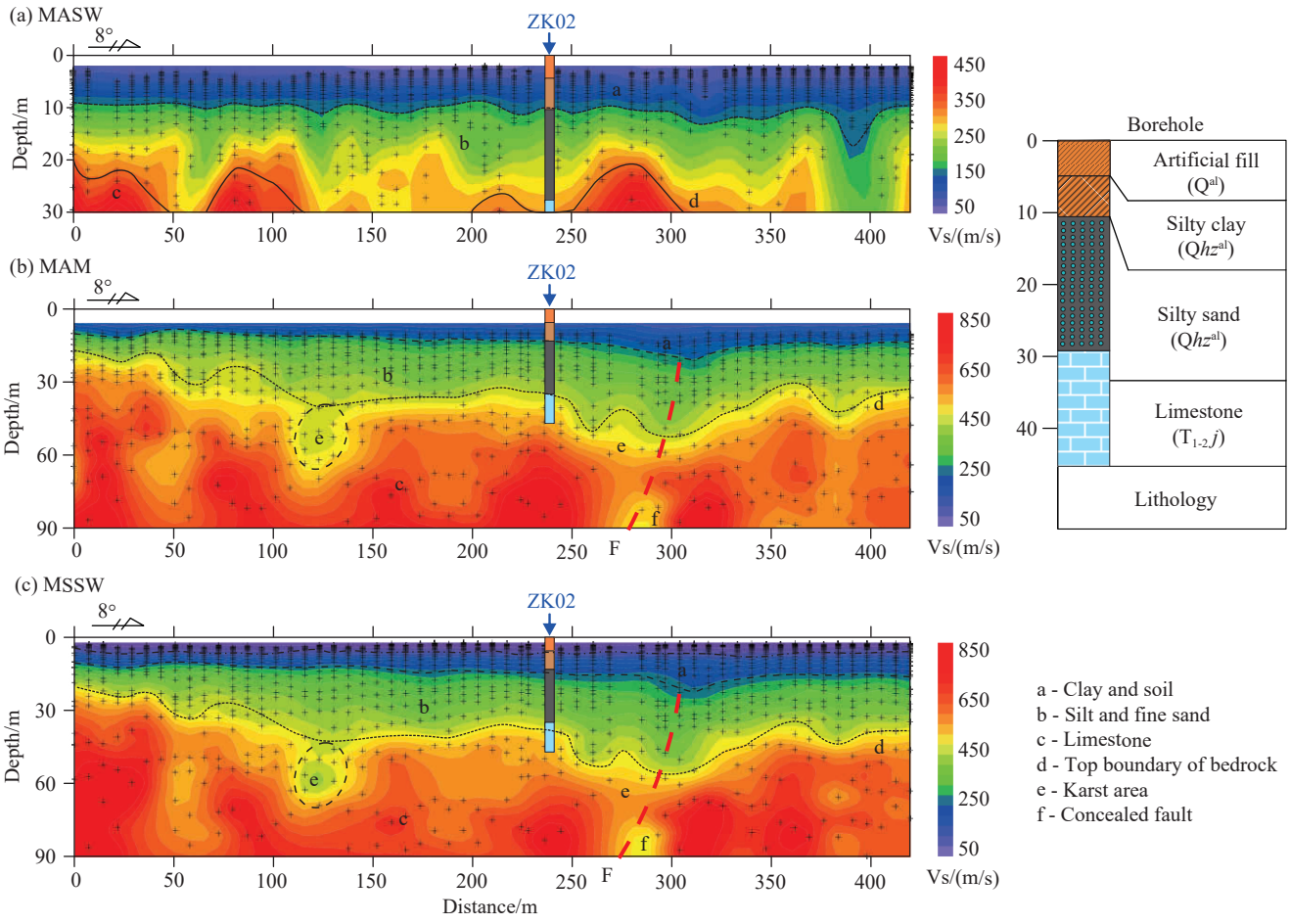

Fig. 9. 2D profile results of three surface wave methods. a–2D profile results of MASW; b–2D profile results of MAM; c–2D profile results of MSSW.

speed anomaly was identified, likely caused by a fault. Therefore, MSSW combines the advantages of active and passive surface wave methods, improving detection depth, construction efficiency, and anomaly visualization. However, it remains susceptible to high-order surface wave signals and interference components in both active and passive signals.

3.3. Ground Penetrating Radar (GPR)

GPR is an RF (0.10–3 GHz) electromagnetic exploration technology based on the differences in the electromagnetic properties of different underground media (dielectric constant, conductivity, and magnetic permeability). GPR is currently the ground geophysical method with the highest detection resolution, characterized by fast scanning speed, wide coverage, and low cost. It is widely used in fields such as urban cable detection, highway survey, karst and cavity detection (Liu LB and Qian RY, 2015).

GPR is a highly effective method for describing the epikarst in detail (i.e. the shallow part of karst systems) and the infiltration zone of karst aquifers, where limestone crops out at the surface (Chalikakis K et al., 2011). In recent years, GPR techniques appear to be the most popular geophysical tools for identifying and locating subsurface karst features such as cavities, conduits and solutionally enlarged fractures (Anchuela OP et al., 2009; Rodriguez V et al., 2014). However, GPR encounters significant limitations in areas where the overburden exhibits high electrical conductivity, which is commonly observed in temperate lowland karst regions characterized by a thick residual clay soil cover, coincidentally similar to the conditions in Wuhan. In this experiment, the TerraSIRch SIR3000 system, manufactured by GSSI in USA, was used to investigate the shallow geological structure in a karst subsidence area located in Fasi Street. The profile was located in a flat farmland area, and a low-frequency 40 M antenna was utilized to acquire point data with a spacing of 0.5 m. RADAN7 software was employed for data processing, which encompassed gain adjustment, filtering, noise reduction, and offset correction. Time-depth conversion was conducted at a velocity of 1.0×10^8 m/s, leading to the detection results presented in Fig. 10.

The analysis and interpretation of GPR detection results reveal distinct characteristics in different geological environments. In the collapsed backfill area, the radar signal exhibits strong chaotic reflections and anomalies, whereas the reflection signal is comparatively weaker in the original continuous sedimentary environment. This discrepancy facilitates the identification of soil disturbances. The application of low frequencies, such as 40 MHz, has proven to be efficient and valuable for GPR investigations in limestone formations due to the minimal attenuation of radar waves. However, the use of non-shielded low-frequency antennas renders the radar signals susceptible to interference from surrounding conductive objects, including electric poles and metal guardrails. Moreover, the presence of a thick loose layer

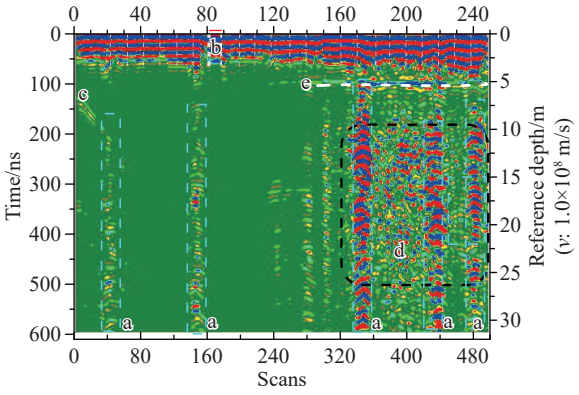

Fig. 10. Results of GPR profile detection.

and abundant groundwater in the shallow subsurface of Wuhan contributes to rapid attenuation of radar waves. To ensure sufficient detection depth in Wuhan, the utilization of a low-frequency antenna is recommended. Nevertheless, it is imperative to identify and eliminate interference resulting from inadequate shielding during data processing and interpretation.

Electromagnetic wave CT (EM CT) mainly uses the absorption of electromagnetic waves in a dissipative medium to reconstruct the electromagnetic absorption coefficient for the purpose of detecting geological anomalies. Currently, this method only measures the electric field signal, and the single-frequency electromagnetic waves typically range from 1 kHz to 10 MHz. Due to lack of travel time data to correct ray path, EM CT imaging between boreholes is mainly performed based on direct line tracing (Liu SX and Ni JF, 2020). Therefore, it has the advantages of simple principle and stable inversion. And with the numerous domestic equipment, EM CT is widely used in engineering bridge and tunnel surveys, isolated rocks, karst detection, and other fields (Li SC et al., 2015).

EM CT for detecting karst had been studied since the early 1960s (Wu YR, 1982), and the general effectiveness has been verified by a large number of cases. Huang SG et al. (2018) revealed the propagation rule of electromagnetic waves inside karst caves through FDTD simulation. And the EM CT experiment in Wuhan was conducted in the karst area of Baishazhou. One pair of two boreholes were used for transmission and reception, with the boreholes spacing of 20 m and a detection depth between 25–53 m. The obtained electromagnetic absorption coefficient was inferred and explained in combination with boreholes data (Fig. 11).

The electromagnetic wave energy detected by the EM CT exhibited a notable decrease as it propagated through the subsurface. Moreover, the absorption rate parameter demonstrated a distinct banded characteristic with depth. Particularly, two zones with significant electromagnetic wave absorption anomalies were identified: one at a depth shallower than 35 m, and the other between 47 m and 51 m, where the absorption rates exceeded 7. These findings align

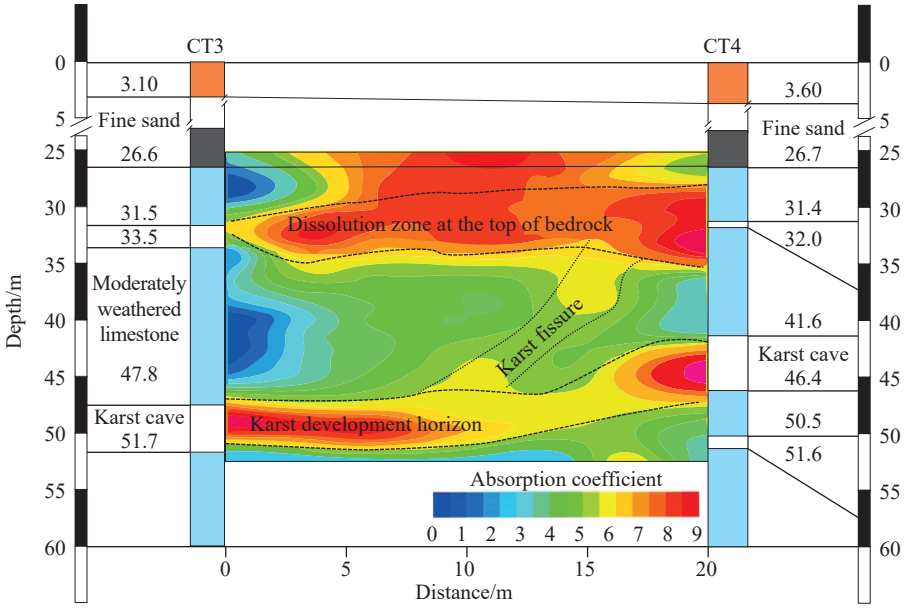

Fig. 11. Results of EM CT detection.

closely with the karst development zone identified through borehole data, indicating the presence of karst development layers both above and below, as well as karst fissures existing between them.

3.4. Opposing-coils Transient Electromagnetic Method (OCTEM)

The Opposing-coils transient electromagnetic method (OCTEM) is a new shallow time-domain electromagnetic exploration method, which uses two sets of parallel coaxial coils as the transmitter and measures the pure secondary field coupled to the center of the earth on the zero magnetic flux plane of the first field generated by the double coil source. This method has the advantages of improving coupling energy, reducing side effects, and increasing lateral resolution (Xi ZZ, et al., 2016). In this study, the OCTEM experiment was conducted in the karst collapse area of Fasi-Street. The instrument used was the HPTEM-18 produced by Hunan Wuwei Geological Technology Co., Ltd. The measurement was performed with 5 m point spacing, a transmission frequency of 6.25 Hz, stacking times of no less than 300 times, and repeat times of no less than 2. The instrument's built-in software was used for data processing, and the transient relaxation inversion method was selected to obtain the resistivity results (Fig. 12).

Combining the drilling data for depth calibration of the results obtained by OCTEM, it can be seen that there are four electrical structure characteristics: The surface clay layer has a resistivity of less than 50 Ω·m, and two sub-high resistance anomalies can be seen inside, which can correspond to the position of the previous subsidence area. The lower sand layer has a resistivity ranging from 50 Ω·m to 350 Ω·m, with a thickness of about 15 m to 25 m. Multiple low resistance anomalies can be seen at the top, indicating the existence of clay entering the sand body. The Permian Qixia Formation

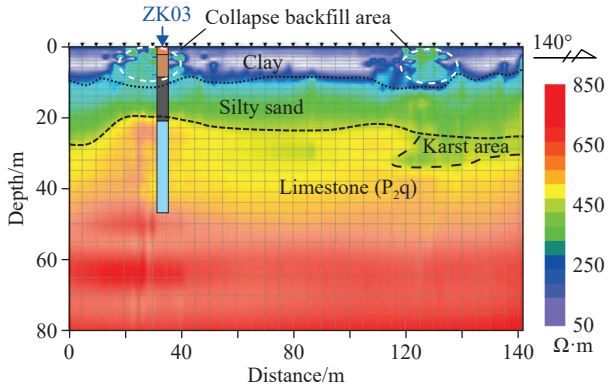

Fig. 12. Results of OCTEM in the karst collapse area.

limestone (P_2q) is the main high- resistivity rock, with a resistivity of over 800 Ω·m, and has a clear double-layer structure, reflecting the existence of weathering at the top. The burial depth of the top interface is between 20 m and 35 m, and no bottom is observed.

3.5. Surface Nuclear Magnetic Resonance (SNMR)

Surface nuclear magnetic resonance (SNMR) is a high-tech geophysical technology developed over the past 30 years that directly detects groundwater with sensitivity, efficiency, and non-destructiveness (Chen B et al., 2014). It generates an excitation magnetic field by supplying an alternating current with a Larmor frequency to a ground coil, causing hydrogen nuclei to undergo a level transition. The nuclear magnetic resonance signal generated by the spontaneous level transition is received to invert the groundwater content and relaxation time with depth. The “dead time” of SNMR instruments can now be shortened to 4 ms, enhancing its ability to identify small-pore water-bearing layers (Walsh D et al., 2014). New technologies such as multi-channel separate coil acquisition systems, reference channels, and adaptive noise reduction

greatly enhance its anti-interference ability (Behroozmand AA et al., 2015; Lin J and Zhang Y, 2016). SNMR is mainly applied in groundwater detection, water resource assessment, and tunnel advance detection (Flinchum BA et al., 2019; Liu DH et al., 2022b).

Fig. 13 shows the SNMR results in the Fashi-Street karst subsidence. The groundwater is relatively abundant and mainly consists of pore water, while karst water is weakly developed. Three aquifers can be identified at depths shallower than 80 m. The first aquifer, located at 1.5–4 m, mainly consists of small-pore bound water that changes significantly with depth. The second aquifer is the main aquifer in the area, distributed at a depth of 8–25 m and consisting of fourth-order pore confined water with a water content of up to 40%. The average transverse relaxation time T_2* indicates a two-layer structure, reflecting the "small on top, large on bottom" porosity characteristic of this section, which corresponds well with the "sticky on top, sandy on bottom" double-layer structure revealed by drilling. The top of the third aquifer is buried at a depth of about 32 m, and the water type is karst fissure water with a maximum water content of 8%. Two anomalies exist at depths shallower than 50 m, indicating that the karst fissure is filled with overlying fine sand. No obvious free water distribution is observed at depths deeper than 50 m, reflecting poorly developed deep karst.

4. Discussion

In recent years, considerable research efforts have been devoted to establishing guidelines for the effective application of geophysical methods in karst system exploration. Thomas B and Roth MJS (1999) conducted a comprehensive study comparing 12 different methods, including four geophysical techniques, for sinkhole and void detection in eastern Pennsylvania and north New Jersey, USA. Hutchinson DJ et al. (2002) provided a valuable comparison of various geophysical approaches for void detection. Fauchard C and Pothérat P (2004) developed a guide for detecting air-filled caves using geophysical methods. Bechtel TD et al. (2007) presented a comprehensive book on karst hydrogeology, describing geophysical methods specifically tailored for karst studies. Gutiérrez F et al. (2008) evaluated the effectiveness of geophysical methods for sinkhole detection in evaporate areas, building on the general utilization of geophysical techniques proposed by Hoover RA (2003) for karst exploration. Additionally, Chalikakis K et al. (2011) evaluated the adequacy of surface-based geophysical methods commonly used in karst-system exploration. These seminal works provide a solid foundation for assessing the suitability of geophysical tools in karst-system exploration.

4.1. Method Suitability

As discussed in Chapter 3, the distinct characteristics of the eight geophysical methods offer improved ways to detect karst formations, with detection depth, resolution, and anti-interference ability playing vital roles (Li XY et al., 2020; Wang X et al., 2021). Building upon the results of the previous experiments, this paper presents qualitative technical indicators for the most common karst-related issues in Table 4. Resolution and anti-interference have been evaluated on four levels: Ultra-high (****), high (***), medium (**), and low (*). Notably, the anti-jamming ability of geophysical methods is crucial in urban geophysical surveys due to the presence of ambient noise. Therefore, careful consideration should be given to appropriate anti-noise technologies, such as multi-arrays joint inversion and the remote reference method.

Furthermore, it is important to acknowledge that the geophysical response is influenced by the size and depth of the target, as well as the contrast in physical properties between the target and the surrounding rock. In Chapter 2,

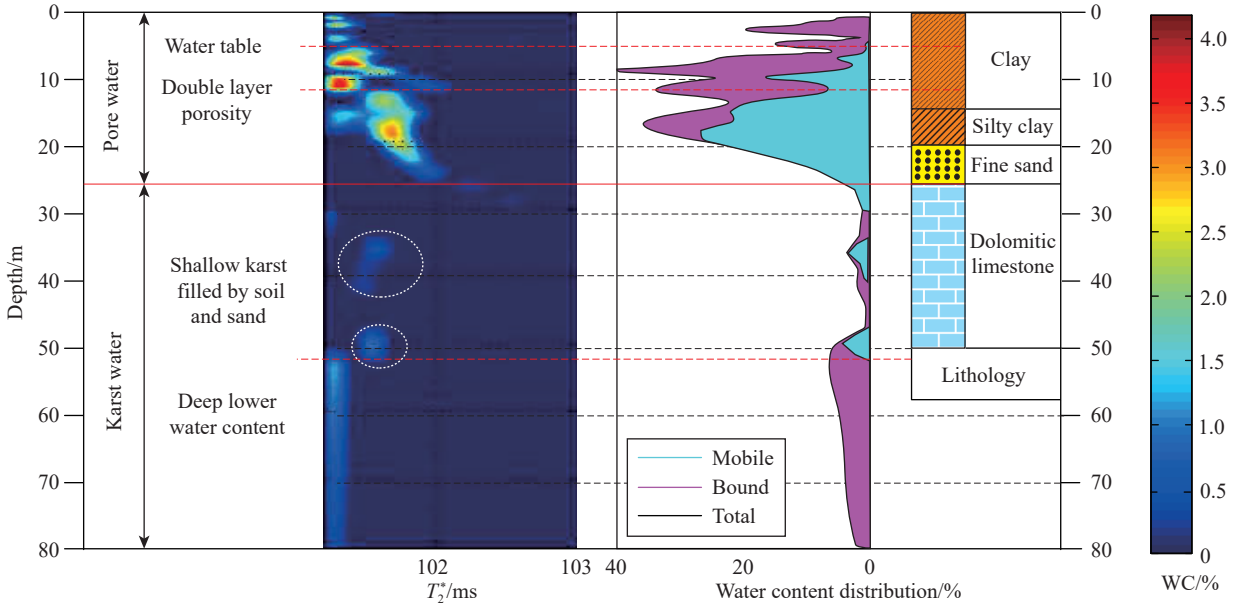

Fig. 13. Results of SNMR in the karst collapse area.

Table 4. Adequacy of geophysics in the karst-system exploration of Wuhan City.

Geophysical methods	Technical characteristics			Adequacy of the methods											
	Depth of detection	Resolution	Anti-interference	Karst						Soil			Groundwater		
				Lithology	Development	Boundaries	Fracture zone	Cavities		Structure	Thickness	Locate disturbance	Type	Aquifer structure	Aquifer properties
								Air-filled	Water-filled						
ERT	0–200 m	***	****	+++	++	++	++	+++	+++	+++	+++	++	+++	++	+
GPR	0–20 m	****	****	-	+	+	+	+	+	++	++	+++	-	-	-
OCTEM	0–200 m	**	**	++	++	++	+++	+	+	++	++	++	+	+++	+
EM CT	Borehole related	***	***	++	+++	++	+++	++	++	++	++	+	+	+	+
MASW	0–20 m	**	***	+	+	+	++	+	+	+++	++	++	++	+++	-
MAM	0–200 m	**	****	+++	++	+	+	+++	+++	-	-	-	-	+	-
MSSW	0–200 m	***	**	+++	++	+	+	+++	+++	++	++	++	-	-	-
SNMR	0–150 m	**	*	-	+	+	-	-	+++	++	++	-	+++	+++	+++

Notes: Resolution: **** ultra-high; *** high; ** medium; * low;
Anti-interference capability: **** extremely strong; *** strong; ** moderate; * weak;
Adequacy: +++ recommended; ++ appropriate but incomplete; + appropriate but limited; - not recommended.

this paper aimed to standardize the main karst-related issues by reviewing the common geological characteristics of karst in Wuhan. The main detection targets were summarized into three aspects related to karst, soil, and groundwater, as shown in Table 2. To summarize the usefulness of the previously mentioned geophysical methods, a classification is proposed: (1) Recommended when multiple studies demonstrate the method's relevance and, in some cases, its standalone capability for characterizing karst-specific targets; (2) appropriate but incomplete when good results are achieved for a specific karst issue but are mostly supplemented by other methods for concrete data interpretation; (3) appropriate but limited when only a few studies show the method's usefulness, even when combined with other methods; and (4) not recommended when the method is not suitable for the geometry and physical properties of the specific target.

Table 4 indicates that ERT is a widely effective geophysical tool for detecting karst-related issues due to its sensitive resistivity indicator. It provides enhanced insights into the lithology of the surrounding rock by engaging with the complete rock mass, and 3D ERT can resolve certain structural features by detecting rock discontinuities. However, in urban geophysical surveys, proper electrode implementation and ensuring adequate contact remain major practical challenges to be addressed. GPR, on the other hand, is primarily used for soil detection in urban areas due to the thicker soil cover and abundant groundwater. Several transducers are utilized in surface wave (SW) methods to effectively remove noise and perform well on urbanized hard ground. MAM and MSSW have proven useful in identifying and locating various karst features such as faults and geological contacts, while MASW is suitable for detecting and imaging near-surface karst structures. SNMR, a relatively new geophysical technique, is developed for groundwater exploration and can be applied to investigate groundwater-related issues, including aquifers and water-filled karst systems. However, it should be noted that these studies are continuously evolving, and the accuracy and applicability of all geophysical methods may vary. Given the distinctive characteristics exhibited by individual karst systems, the applicability of geophysical methods may vary depending on site-specific conditions. Therefore, conducting preliminary experiments in the study area prior to the survey is highly recommended. This is crucial to assess the suitability and appropriateness of the selected methods or measuring techniques.

4.2. Construction of Multiple Geophysical Method Combinations for Karst Detection in Wuhan

As shown in Table 4, for each karst-related issue, there are diverse karst exploration targets composed of three aspects as karst, soil, and groundwater, which is difficult for one geophysical method to give satisfactory results. The use of a combination of geophysical tools is always preferable to obtain a better constrained model of karst features (Lü QT et al., 2019). Due to the inevitable ambient noise and the dense

buildings, it is always challenging to conduct geophysical surveys in urban (Li WL et al., 2018), especially in built-up areas. Conversely, in newly developed areas, the selection of geophysical methods is more flexible due to larger spaces and lower ambient noise levels.

Karst collapse represents a common geological hazard in concealed karst areas and can be divided into three stages: karst development, collapse formation, and collapse treatment (He J et al., 2020). In the karst development stage, dissolution phenomenon gradually form, and the soil layer remains unaffected. It's recommended to employ MAM and large-scale ERT to rapidly delineate the karst areas and identify hydrogeological conditions with assistance from SNMR. During the collapse formation stage, karst cavities enlarge and become filled, resulting in the formation of soil caves. For investigating the distribution of soil caves and characterizing doline geometry, GPR, MSSW, and medium-scale ERT are recommended. In the collapse and treatment stage, collapse events have occurred, and geophysical detection primarily aims to understand the collapse mechanism and assist in geological disaster control. Consequently, geophysical methods with higher resolutions, such as GPR and EM CT, are recommended, with MSSW and 3D ERT serving as supplementary techniques (Table 5).

Geophysical methods have been widely used in karst-related investigations, among which there are three main application scenarios: Geological survey, engineering investigation and hazard treatment (Table 5). Firstly, in the fundamental karst geological survey scenario, geophysical detection has been carried out for urban planning to put forward reasonable design and construction scheme, in which the scale is usually less than 1∶10000, and it's recommended to use MAM and large-scale ERT to rapidly delineate the karst areas and identify buried or hidden preferential pathways, and combining with SNMR to detect the hydrogeological conditions. Secondly, in the engineering investigation scenario, for field geophysical exploration of the scale of the site, to distinguish more fractured zones and identify karst cavities, EM CT, small-scale ERT, GPR, and MAM are recommended, assisted by MSSW and OCTEM. Thirdly, to support the emergency investigations for disaster management, the shallow structural information of epikarst and soil layer needs to describe in detail. It is recommended to use GPR, small-scale 2D ERT and 3D ERT to identify and locate subsurface karst features such as cavities, conduits and solutionally enlarged fractures.

5. Conclusions

(i) In Wuhan, there are eight karst belts that extend in an east-west direction, covering an approximate area of 1162 km^2. The majority of these regions, constituting 96%, are concealed karst areas. The karst formations primarily comprise four sets of limestone and dolomite from the Carboniferous, Permian, and Triassic periods. Among these, the karst developed during the Permian period appears to be the most prominent. The karst phenomena in these areas are predominantly characterized by medium to small-sized caves and dissolution cavities filled with mud and sand. These features are buried beneath overburden sediments ranging from 30 m to 50 m in thickness and are surrounded by saturated groundwater.

(ii) This paper evaluates the feasibility of eight geophysical methods in karst systems based on field experiments conducted in Wuhan. Among these methods, ERT has shown extensive applicability in detecting karst-related issues. It is recommended to utilize joint inversion of multi-arrays and 3D ERT for improved imaging results. However, proper implementation of electrodes and ensuring adequate contact present significant practical challenges in urban surveys. Due to the presence of thick clay and groundwater in Wuhan, GPR is limited but capable of swiftly identifying disturbed soil and cavities in overburden sediments. MSSW enhances the detection capabilities of MAM and MASW, making it suitable for urban karst detection. Additionally, SNMR is a sensitive technique for groundwater exploration, specifically designed to investigate aquifers and water-filled karst systems.

(iii) The karst collapse in Wuhan is influenced by the intricate interaction of soluble rock, groundwater, and soil. Due to the complex geometries of these factors, effectively exploring them with a single geophysical method poses challenges. Therefore, it is recommended to combine multiple geophysical methods to enhance detection effectiveness. This study provides specific recommendations for the integration of geophysical methods, serving as a reference for concealed karst detection in Wuhan.

CRediT authorship contribution statement

Dao-han Liu, Lei Wang conceived of the presented idea.

Table 5. Suggestion of combination scheme of geophysical methods in Wuhan City.

Geophysical service objects		Urban built-up area		Development area		Geophysical methods
		Primary combination	Secondary combination	Primary combination	Secondary combination	
Collapse stages	Karst development	①+⑤	③+⑤	①+⑤+⑧	①+⑧	① ERT ② GPR ③ OCTEM ④ MASW ⑤ MAM ⑥ MSSW ⑦ EM CT ⑧ SNMR
	Collapse formation	②+⑥	①+②+⑥	①+②+⑧	①+②+⑥	
	Collapse treatment	②+⑦	①+②	②+⑦	①+②+⑥	
Geological scenarios	Geological survey	①+⑤	③+⑤	①+⑧	⑤+⑧	
	Engineering investigation	②+⑤+⑦	①+②+⑦	①+⑥+⑦	①+⑤+⑦	
	Hazard treatment	①+②	②+③	①+②	②+⑤	

Dao-han Liu, Lei Liu, and Jian-Qiang Wu completed the study of section inversion and comparative analysis. Dao-han Liu wrote the manuscript under supervision of Jun-jie Xu, Jian-Qiang Wu, Lei Liu, Lei Wang, and Pan Liu. Jian-Qiang Wu and Jun-jie Xu helped the English polishing of the manuscript. All authors discussed the results and contributed to the final manuscript.

Declaration of competing interest

The authors declare no conflicts of interest.

Acknowledgement

This research was jointly supported by the project of Chinese National Natural Science Foundation (42107485), National Key R&D Program (2020YFC1512400, 2018YFC800804) and China Geological Survey (DD20190282, DD20221734, and DD20230323). The authors would like to thank Zhen-yu Li, Tie Liu, Song Chen, Xue-ming Shi, and Zhen-zhu Xi for their detailed and constructive comments.

References

Anchuela OP, Casas-Sainz AM, Soriano MA, Pocoví-Juan A. 2009. Mapping subsurface karst features with GPR: Results and limitations. Environmental Geology, 58, 391–399. doi: 10.1007/s00254-008-1603-7.

Bechtel TD, Bosch FP, Gurk M. 2007. Geophysical methods. Methods in karst hydrogeology, 171–199.

Behroozmand AA, Keating K, Auken E. 2015. A Review of the Principles and Applications of the NMR Technique for Near-Surface Characterization. Surveys in Geophysics, 36(1), 27–85. doi: 10.1007/s10712-014-9304-0.

Chalikakis K, Plagnes V, Guerin R, Valois R, Bosch FP. 2011. Contribution of geophysical methods to karst-system exploration: An overview. Hydrogeology Journal, 19, 1169–1180. doi: 10.1007/s10040-011-0746-x.

Chen BD, Li X, Li ZC, Jiang C, Jia Y, Li HJ, Liu PR. 2021. Classification of geological structure and karst collapse in concealed karst area of Wuhan Baishazhou, Hubei. The Chinese Journal of Geological Hazard and Control, 32(02), 43–52 (in Chinese with English abstract). doi: 10.16031/j.cnki.issn.1003-8035.2021.02.06.

Chen B, Hu XY, Liu DH, Zhang YX. 2014. The development history and new progress of magnetic resonance sounding technique. Progress in Geophysics, 29(2), 650–659 (in Chinese with English abstract).

Chen YL, Gan FP, Lu CJ, Wei JY, Zhao W. 2013. The study of underground river course detection by integrated geophysical methods in bare karst area. Progress in Geophysics, 28(3), 1608–1616 (in Chinese with English abstract).

Constantin P, Kurosch T, Michael K, Reinhard S. 2019. Testing the effectiveness of an inverse Wenner-Schlumberger array for geoelectrical karst void reconnaissance, on the Swabian Alb high plain, new line Wendlingen, southwestern Germany. Engineering Geology, 249, 71–76. doi: 10.1016/J.ENGGEO.2018.12.014.

Eftychia A, George V, Panagiotis T. 2022. Combined application of seismic and electrical geophysical methods for karst cavities detection: A case study at the campus of the new University of Western Macedonia, Kozani, Greece. Journal of Applied Geophysics, 196, 144–156. doi: 10.1016/j.jappgeo.2021.104499.

Fan SK. 2006. A discussion on karst collapse in Wuhan (Hubei). Resources Environment and Engineering, (S1), 608–616 (in Chinese with English abstract). doi: 10.16536/j.cnki.issn.1671-1211.2006.s1.005.

Fauchard C, Pothérat P. 2004. Detection of underground cavities by geophysical techniques. Guide technique, Laboratoire Central des Ponts et Chaussées, Paris, 170.

Flinchum BA, Holbrook WS, Parsekian AD, Carr AJ. 2019. Characterizing the critical zone using borehole and surface nuclear magnetic resonance. Vadose Zone Journal, 18(1), 124–131. doi: 10.2136/vzj2018.12.0209.

Fu ZY, Ren ZY, Hua XR, Shi Y, Chen H, Chen CJ, Li YN, Tang JT. 2020. Identification of underground water-bearing caves in noisy urban environments (Wuhan, China) using 3D electrical resistivity tomography techniques. Journal of Applied Geophysics, 174. doi: 10.1016/j.jappgeo.2020.103966.

Gambetta M, Armadillo E, Carmisciano C, Stefanelli P, Cocchi L, Tontini FC. 2011. Determining geophysical properties of a near-surface cave through integrated microgravity vertical gradient and electrical resistivity tomography measurements. Journal of cave and karst studies, 73, 11–15. doi: 10.4311/jcks2009ex0091.

Gan F, Han K, Lan F, Chen Y, Zhang W. 2017. Multi-geophysical approaches to detect karst channels underground — a case study in Mengzi of Yunnan Province. Journal of Applied Geophysics, 136, 91–98. doi: 10.1016/j.jappgeo.2016.10.036.

Gutiérrez F, Cooper HA, Johnson KS. 2008. Identifification, prediction and mitigation of sinkhole hazards in evaporate karst areas. Environmental Geology, 53, 1007–1022. doi: 10.1007/s00254-007-0728-4.

He J, Liu L, Li QH, Liu DH, Chen BD, Zhang A, Zhao YB. 2020. Study on technique and method of underground space exploration in concealed karst area: A case study of Wuhan. Hydrogeology and Engineering Geology, 47(6), 47–56 (in Chinese with English abstract). doi: 10.16030/j.cnki.issn.1000-3665.202007066.

Hoover RA. 2003. Geophysical choices for karst investigations. Sinkholes and the engineering and environmental impacts of karst. American Society of Civil Engineers, Reston, 529–538. doi: 10.1061/40698(2003)48.

Huang SG, Liu DJ, Hu YJ. 2018. Simulation analysis and application study of electromagnetic wave computed tomography in detecting karst caves. Rock and Soil Mechanics, 39(S1), 544–550 (in Chinese with English abstract). doi: 10.16285/j.rsm.2017.2292.

Hutchinson DJ, Phillips C, Cascante G. 2002. Risk considerations for crown pillar stability assessment for mine closure planning. Geotechnical & Geological Engineering, 20, 41–64. doi: 10.1023/A:1013852722768.

Ismail A, Anderson N. 2012. 2-D and 3-D resistivity imaging of karst sites in Missouri, USA. Environmental & Engineering Geoscience, 18(3), 281–293. doi: 10.2113/gseegeosci.18.3.281.

Kaufmann O, Deceuster J. 2014. Detection and mapping of ghost-rock features in the Tournaisis area through geophysical methods —an overview. Geologica Belgica, 17(1), 17–26.

Li CX, Liu L, Zhou SC, Wang BZ. 2021. Application of geophysical prospecting technology in karst collapse disaster monitoring and early warning. Resources Environment and Engineering, 35(06), 887–894 (in Chinese with English abstract). doi: 10.16536/j.cnki.issn.1671-1211.2021.06.020.

Li SC, Liu ZY, Liu B, Xu XJ, Wang CW, Nie LC, Sun HF, Song J, Wang SR. 2015. Boulder detection method for metro shield zones based on cross-hole resistivity tomography and its physical model tests. Chinese Journal of Geotechnical Engineering, 37(3), 446–457 (in Chinese with English abstract). doi: 10.11779/CJGE201503008.

Li SC, Wang K, Li LP, Zhou ZQ, Shi SS, Liu S. 2017. Mechanical mechanism and development trend of water-inrush disasters in karst tunnels. Chinese Journal of Theoretical and Applied Mechanics, 49(1), 22–30 (in Chinese with English abstract). doi: 10.6052/0459-1879-16-345.

Li WL, Liu SF, Tian QN, Lv P, Jiang ZX, Jia LX. 2018. A review of urban geophysics. Progress in Geophysics, 33(5), 2134–2140 (in Chinese with English abstract). doi: 10.6038/pg2018BB0463.

Li XY, Chen XF, Yang ZT, Wang B, Yang B. 2020. Application of high-order surface waves in shallow exploration: An example of the Suzhou River, Shanghai. Chinese Journal of Geophysics, 63(1), 247–255 (in Chinese with English abstract). doi: 10.6038/cjg2020

N0202.
Lin J, Zhang Y. 2016. Research status and prospect of ground nuclear magnetic resonance water exploration. Chinese Journal of Scientific Instrument, 37(12), 2657–2670 (in Chinese with English abstract). doi: 10.19650/j.cnki.cjsi.2016.12.003.
Liu LB, Qian RY. 2015. Ground Penetrating Radar: A critical tool in near-surface geophysics. Chinese Journal of Geophysics, 58(8), 2606–2617 (in Chinese with English abstract). doi: 10.6038/cjg20150802.
Liu DH, Xu JJ, Liu L, He J, Qi x, Chen S. 2022a. Application of the integrated geophysical methods in the fine exploration of karst collapses: A case study of Wuhan. Geology and exploration, 58(04), 865–874 (in Chinese with English abstract). doi: 10.12134/j.dzykt.2022.03.000.
Liu DH, Zhang X, He J, Wu J, Liu L. 2022b. Study on the application of surface nuclear magnetic resonance in the detection of karst collapse in Wuhan. Carsologica Sinica, 41(01), 13–20 (in Chinese with English abstract). doi: 10.11932/karst202201.
Liu SX, Nie JF. 2020. Review for cross-hole electromagnetic method. Progress in Geophysics, 35(1), 153–165 (in Chinese with English abstract). doi: 10.6038/pg2020DD0088.
Luo XJ, Luo C. 2021. Three-Mechanism Theory (TMT) of karst ground collapse and its application. Carsologica sinica, 40(2), 171–188 (in Chinese with English abstract). doi: 10.11932/karst2021y001.
Lü QT, Zhang XP, Tang JT, Jin S, Liang LZ, Niu JJ, Wang XB, Lin PR, Yao CL, Gao WL, Gu JS, Han LG, Cai YZ, Zhang JC, Liu BL, Zhao JH. 2019. Review on advancement in technology and equipment of geophysical exploration for metallic deposits in China. Chinese Journal of Geophysics, 62(10), 3629–3664 (in Chinese with English abstract). doi: 10.6038/cjg2019N0056.
Meng Y, Lei MT. 2019. Current situation and trend analysis of karst collapse research. Carsologica Sinica, 38(3), 411–417 (in Chinese with English abstract). doi: 10.11932/karst20190311.
Peng JB, Huang WL, Wang FY, Liu Y. 2019. Geological structural classification of and geological survey method for urban underground space in China. Earth Science Frontiers, 26(3), 9–21 (in Chinese with English abstract). doi: 10.13745/j.esf.sf.2019.5.34.
Peng Y, Dong YP, Fan YS, Xu LZ, Zhao XG. 2016. Application of the electromagnetic CT in Karst exploration of T1d in Wuhan. CT Theory and Applications, 25(4), 419–424 (in Chinese with English abstract). doi: 10.15953/j.1004-4140.2016.25.04.05.
Rodriguez V, Gutiérrez F, Green AG, Carbonel D, Horstmeyer H, Schmelzbach C. 2014. Characterizing sagging and collapse sinkholes in a mantled karst by means of ground penetrating radar (GPR) characterizing mantled karst sinkholes by GPR. Environmental and Engineering Geoscience, 20(2), 109–132. doi: 10.2113/gseegeosci.20.2.109.
Solbakk T, Fichler C, Wheeler W, Lauritzen S, Ringrose P. 2018. Detecting multiscale karst features including hidden caves using microgravimetry in a Caledonian nappe setting: Mefjell massif, Norway. Norsk Geologisk Tidsskrift, 98(3), 359–378. doi: 10.17850/njg98-3-04.
Thomas B, Roth MJS. 1999. Evaluation of site characterization methods for sinkholes in Pennsylvania and New Jersey. Engineering Geology, 52(1–2), 147–152. doi: 10.1016/S0013-7952.
Ungureanu C, Priceputu A, Bugea AL, Chiric A. 2017. Use of electric resistivity tomography (ERT) for detecting underground voids on highly anthropized urban construction sites. Procedia Engineering, 209, 202–209. doi: 10.1016/j.proeng.2017.11.148.
Valois R, Camerlynck C, Dhemaied A, Guerin R, Hovhannissian G, Plagnes V, Rejiba F, Robain H. 2011. Assessment of doline geometry using geophysics on the Quercy plateau karst (South France): Morphology of dolines using geophysics. Earth Surface Processes & Landforms, 36(9), 1183–1192. doi: 10.1002/esp.2144.
Verdet C, Sirieix C, Marache A, Riss J, Portais JC. 2020. Detection of undercover karst features by geophysics (ERT) Lascaux cave hill. Geomorphology, 360(1), 167–177. doi: 10.1016/j.geomorph.2020.107177.
Walsh D, Grunewald E, Turner P, Hinnell A. 2014. Surface NMR instrumentation and methods for detecting and characterizing water in the vadose zone. Near Surface Geophysics, 12(2), 271–284. doi: 10.3997/1873-0604.2013066.
Wang CS, Zhou CH, Peng JB, Fan J, Zhu HH, Li XZ, Cheng GH, Dai CS, Xu NX. 2019. A discussion on high-quality development and sustainable utilization of China's urban underground space in the new era. Earth Science Frontiers, 26(3), 1–8 (in Chinese with English abstract). doi: 10.13745/j.esf.sf.2018.9.2.
Wang F, Chai B, Xu GL, Chen L, Xiong ZT. 2017. Study on the evolution mechanism of karst collapse in Wuhan. Journal of Engineering Geology, 25(3), 824–832 (in Chinese with English abstract). doi: 10.13544/j.cnki.jeg.2017.03.030.
Wang JX, Yang LZ, He J. 2001. The coupling interaction of groundwater-soil-rock mass in karst collapse evolution. Journal of Southwest Jiaotong University, 14(3), 314–317 (in Chinese with English abstract).
Wang LM, Xia JH, Luo YH, Bian AF. 2022. Progress and prospect of surface-wave imaging techniques in near-surface applications. Reviews of Geophysics and Planetary Physics, 53(6), 613–655 (in Chinese with English abstract). doi: 10.19975/j.dqyxx.2022-008.
Wang X, Wang ZH, Chen CX, Wang H, Yan JY. 2021. Geophysical exploration and application for urban underground space. Progress in Geophysics, 36(5), 2204–2214 (in Chinese with English abstract). doi: 10.6038/pg2021EE0497.
Wu AM, Ma F, Wang GL, Liu JX, Hu QY, Miao QZ. 2018. A study of deep-seated karst geothermal reservoir exploration and huge capacity geothermal well parameters in Xiongan New Area. Acta geoscientica sinica, 39(05), 523–532(in Chinese with English abstract). doi: 10.3975/cagsb.2018.071104.
Wu YR. 1982. Borehole electromagnetic wave method. Geological Publishing House (in Chinese).
Xi ZZ, Long X, Zhou S, Huang L, Song G, Hou HT, Wang L. 2016. Opposing coils transient electromagnetic method for shallow subsurface detection. Chinese Journal of Geophysics, 59(9), 3428–3435 (in Chinese with English abstract). doi: 10.6038/cjg20160925.
Xu PF, Du YN, Ling SQ, You ZW, Yao J, Zhang H. 2020. Microtremor survey method based on inversion of the SPAC coefficient of multi-mode Rayleigh waves and its application. Chinese Journal of Geophysics, 63(10), 3857–3867(in Chinese with English abstract). doi: 10.6038/cjg202000148.
Yan DP, Pei LZ, Zhang HX, Wang JT, Xu K, Yu SW, Han DC. 2015. Report on the three -dimensional Geological Survey Achievements of the Wuhan City Group in the Middle of the Yangtze River. Wuhan Center, China Geological Survey, 55–58 (in Chinese with English abstract).
Yan JY, Meng GX, Lü QT, Zhang K, Chen XB. 2012. The progress and prospect of the electrical resistivity imaging survey. Geophysical and Geochemical Exploration, 36(4), 576–584 (in Chinese with English abstract).
Yang WC, Tian G, Xia JH, Bao XW, Wang BB, Shi ZJ, Yang B, Zhao WK, Mi BB. 2021. Study on geophysical methods and technologies of underground space survey in Hangzhou area. East China Geology, 42(02), 125–136 (in Chinese with English abstract). doi: 10.16788/j.hddz.32-1865/P.2021.02.001.
Zhang W, Gan FP, Wei W, Guan ZD, Liu W, Wu JQ. 2019. Applied research of comprehensive geophysical method to the investigation of karst collapse in the riverside shoal of Huaihe River. Progress in Geophysics, 34(2), 832–839 (in Chinese with English abstract). doi: 10.6038/pg2019CC0051.
Zheng XM, Jin XG, Liu PR, Yang GX, Li HT, Yang T. 2019. Genesis mechanism and collapse model of karst collapse in Wuhan, Hubei Province. The Chinese Journal of Geological Hazard and Control, 30(5), 75–82 (in Chinese with English abstract). doi: 10.16031/j.cnki.issn.1003-8035.2019.05.10.
Zheng ZJ, Zeng J, Zhao W, Gan FP. 2019. Application research of high density resistivity method in water exploring in karst area. Progress in Geophysics, 34(3), 1262–1267 (in Chinese with English abstract). doi: 10.6038/pg2019CC0190.
Zhu J, James C, James D. 2011. Challenges of using electrical resistivity method to locate karst conduits-a field case in the Inner Bluegrass Region, Kentucky. Journal of Applied Geophysics, 75(3), 523–530. doi: 10.1016/j.jappgeo.2011.08.009.